*Engineering Applications of Computational Fluid Mechanics*, 2015
Vol. 9, No. 1, 12–20, http://dx.doi.org/10.1080/19942060.2015.1004788



# Simulations and measurements of automotive turbocharger compressor whoosh noise

A. Broatch[a], J. Galindo[a], R. Navarro[a]*, J. García-Tíscar[a], A. Daglish[b] and R. K. Sharma[b]

[a]*CMT - Motores Térmicos, Universitat Politècnica de València, Camino de Vera S/N, 46022 Valencia, Spain;* [b]*Jaguar Land Rover Limited, Abbey Road, Whitley, Coventry CV3 4LF, UK*

(*Received 4 April 2014; final version received 4 December 2014*)

Turbocharger noise has become a major concern in downsized automotive engine development. In this paper, the analysis is focused on the *whoosh noise* produced by the compressor when it is working near surge. A centrifugal compressor has been acoustically characterized on a turbocharger test rig mounted on an anechoic chamber. Three in-duct pressure signals forming a linear array are registered in order to obtain pressure components. In this way, meaningful pressure spectra and sound intensity level (SIL) compressor maps are obtained, showing an increase of SIL in the frequency window corresponding to whoosh noise. Besides, detached eddy simulations (DES) of the centrifugal compressor flow in two operating conditions near surge are performed. Good agreement is found between the experimental measurements and the CFD solutions in terms of predicted pressure spectra. Flow analysis is used to identify patterns responsible for the different features of the pressure spectra. At the simulated conditions, rotating instabilities in the compressor diffuser and inducer cause pressure oscillations in the frequency range of whoosh noise.

**Keywords:** CFD; aeroacoustics; rotating stall; centrifugal compressor; DES



## 1. Introduction

Turbocharging has been one of the enablers of automotive powerplants improvement in the last two decades. Nowadays almost all automotive diesel engines and more and more petrol engines are boosted with a turbocharger. Turbocharging, initially conceived as a means to increase the fresh charge within the cylinders, is now the responsible to reduce fuel consumption and pollutant emissions through downsizing and downspeeding (Knecht, 2008). This means that a smaller engine working at increased load and reduced speed can lead to meaningful improvements in consumption and emissions. However, this can only be carried out by increasing the boosting pressure with a turbocharger. Furthermore, the downsizing and downspeeding trends lead the turbomachinery used toward tighter requirements, particularly, in terms of flow range. In order to enlarge the flow range in the compressor from lower surge limit to higher choked flows, several techniques have emerged to reduce the surge limit flow such as ported shroud (Semlitsch et al., 2014) or improved compressor entry designs (Serrano, Margot, Tiseira, & García-Cuevas, 2013). However, the stable working area gained in this process results to be quite noisy (Evans & Ward, 2006). The issue, particularly for high-end automotive brands, is not only the overall acoustic output of turbochargers, but its quality. In particular, an undesirable noise identified as "whoosh" is detected in regions of near surge operation. Whoosh noise is usually identified as a broadband elevation in the medium frequency range between 1 and 3 kHz.

Evans and Ward (2006) found that whoosh noise is most likely to be encountered by the driver during high load acceleration typically below 2500 rpm or during transient tip-out or tip-in maneuvers, associated with operation of the turbocharger compressor close to the surge line. However, whoosh noise was not encountered at the area where operating line is closest to the surge line but at the region of the compressor map where, for a constant speed, the pressure ratio across the compressor increases with increasing mass flow rate. Particularly, the compressor outlet hose was found to be the main source of radiated noise. Teng and Homco (2009) investigated radiated noise on a powertrain dyno in a semi-anechoic cell measured at full load conditions. Improvement of the compressor surge margin was sought so as to reduce whoosh noise, either changing compressor trim or using pre-whirl devices. Additionally, the effects of various resonators at different locations of the intake line on whoosh noise attenuation were studied.

Mendonça, Baris, and Capon (2012) conducted a numerical study regarding flow-induced acoustics of an automotive centrifugal compressor. Sound pressure level (SPL) spectra were obtained for points in both inlet and outlet ducts. Two main features can be observed in the spectra: the blade passing frequency (BPF) tonal noise and a narrow band noise at a frequency about 70% of

*Corresponding author. Email: ronagar1@mot.upv.es

rotational speed. A spiral mode propagating upstream from the compressor impeller is detected for the narrow band noise aforementioned. Velocity vectors on the impeller flow-field revealed leading-edge separation and stalled passages, whereas velocity contours showed a low momentum region that rotates at a slower speed than the wheel. Therefore, inducer rotating stall was found to be the source of the narrow band noise.

Figurella et al. (2012) studied the acoustic and performance characteristics of a turbocharger compressor on a steady-flow turbocharger test bench. Near choke, the compressor noise was dominated by the rotor-order frequency and its harmonics (including BPF). As the flow rate was reduced (thus decreasing the slope of the speed lines) the compressor exhibited a broadband elevation of noise in the 4–12 kHz band. When the mass flow rate is less than a critical value, the temperature near the inducer tips increased sharply, suggesting local flow reversal, and the total SPL in the 4–12 kHz range suddenly reduced.

The bibliographic review shows that whoosh noise is commonly described as a broadband noise either in the 1 kHz–3 kHz band (Gaudé et al., 2008; Lee, Selamet, Kim, Kim, & Kim, 2009; Sevginer, Arslan, Sonmez, & Yilmaz, 2007) or in frequencies ranging from 4 kHz to 12 kHz (Figurella et al., 2012; Karim, Miazgowicz, Lizotte, & Zouani, 2013; Teng & Homco, 2009). Figurella et al. (2012) pointed out that the former could be related to Diesel engines whereas the latter correspond to turbochargers installed in gasoline engines.

In the literature, approaches to the understanding of the mechanism appear to be either purely experimental (Evans & Ward, 2006; Figurella et al., 2012; Teng & Homco, 2009) or essentially computational (Karim, Miazgowicz, Lizotte, & Zouani, 2013; Lee, Selamet, Kim, Kim, & Kim, 2009). The objective of this paper is to combine both techniques to attain a greater understanding of this particular phenomenon.

## 2. Experimental tests

The first stage of the present study consisted in the experimental characterization of the turbocharger aeroacoustic output across a representative region of the operation maps. To do so, the turbocharger was fitted in a turbocharger test rig that was built inside a large anechoic chamber, as depicted in Figure 1. The turbocharger test rig is described in detail by Galindo, Serrano, Guardiola, and Cervelló (2006). The rig is powered by a large Diesel engine capable of producing up to 250 kW. The engine powers a screw compressor, which is used to supercharge the engine itself and also provide pressurized air to a turbocharger turbine located in an adjacent anechoic chamber. The turbine drives the centrifugal compressor that is analyzed in this paper. This anechoic chamber is of the Wedge type, rated with a low cut-off frequency of 100 Hz, thus guaranteeing acoustical free-field conditions above this frequency, which is well below the frequency window of interest (1 kHz to 3 kHz).

Desired operation condition of the turbocharger was achieved by regulating a backpressure valve in the outlet pipe and adjusting the power output of the rig engine, which controls the air mass flow, pressure and temperature of the flow provided to the turbine. However, the operation of this rig is restricted to steady points, lacking the ability to run preprogrammed routines. This limitation was overcome during this study through the use of numeric cubic interpolation between all the recorded data points to obtain a fitted model for

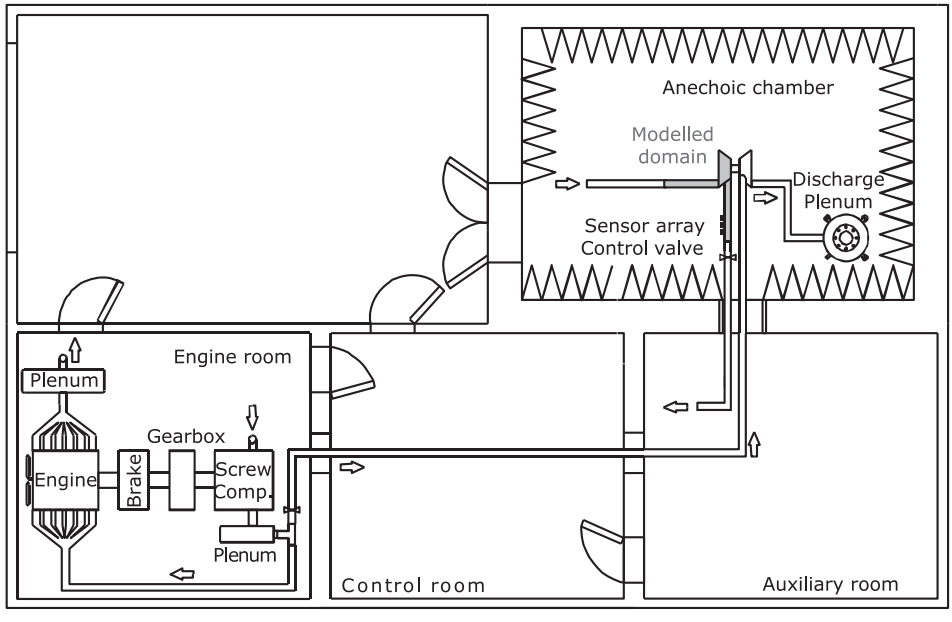


Figure 1. Schematic of the experimental installation.

the whole region. Then, this model can be applied to simulate routines such as a mass flow sweep at constant speed or even the lug line of the actual vehicle application.

Turbocharger status was constantly monitored through pressure, temperature, rotational speed and mass flow sensors, connected to a custom control interface. Using this interface, the operating condition (total-to-total pressure ratio and air mass flow) of the turbocharger could be adjusted and registered.

Besides, an array of three piezoelectric pressure sensors was flush mounted on the outlet pipe of the turbocharger, enabling the attainment of both direct pressure spectra and pressure wave decomposition. Instrumentation *inside* the compressor with pressure transducers as performed by Raitor and Neise (2008) was not considered due to the reduced size of the turbocharger compressor studied. A sketch of the compressor piping is shown in Figure 2, including the linear array. The sensor array was sampled by a standalone Yokogawa DAQ system at 100 kHz using independent channels.

A LCMV beamforming wave decomposition algorithm presented by Piñero, Vergara, Desantes, and Broatch (2000) was used to isolate the components of pressure signal. Then, in-duct sound intensity can be computed as described by Morfey (1971):

$$I = \frac{1}{\rho a}\left(|p_f|^2(1+M)^2 - |p_b|^2(1-M)^2\right) \qquad (1)$$

where $\rho$ is the mean density of the flow, $a$ is the mean sound speed, $p_f$ and $p_b$ are the forwards and backwards pressure spectra, and $M$ is the mean Mach number. This expression enables the calculation of the in-duct sound intensity taking into account the often neglected effect of the mean flow.

However, the beamforming decomposition algorithm is not without limitations. One of the most restrictive is spatial aliasing. The sensor spacing (32 mm; see Figure 2) defines a Nyquist-type upper frequency cut-off that is below the onset of first higher-order acoustic mode due to spatial aliasing effects, as the distance between them implies a time delay, which has an associated limiting frequency. The closer the sensors are placed to each other the higher this limit becomes, but the differences of long-wavelength pressure components between two consecutive sensors diminish, falling eventually below the sensitivity of the sensor, thus imposing a low frequency cut-off as well. For our study, a safe window between 100 Hz and 6 kHz was considered when performing wave decomposition.

Intensity spectra were calculated using Equation 1 and integrated along the frequency band of interest (1–3 kHz) to obtain the overall intensity level of each of the tested operation points. Interpolating these data, it was possible to compute a "noise map" of the compressor, present in Figure 3, similar to others available in the literature Gaudé et al. (2008). Noise level increases with decreasing mass flow, with a steeper gradient (contour lines are close together) near the points with maximum compression ratio at each speed (Evans & Ward, 2006). These points, which present zero isospeed slope, are plotted in the dashed line of Figure 3.

Moreover, spectra of the data points recorded at the 160 krpm isospeed line were also interpolated in order to reconstruct the pseudo spectrogram included in Figure 3, analyzing not only the overall intensity, but its frequency distribution as well. It was found that the so-called whoosh phenomena appeared between 1 kHz and 2.5 kHz at much higher mass flow than the start of the low-frequency phenomena associated to the onset of surge.

Then, two points at different mass flows (59 g/s and 77 g/s) were considered. The latter corresponds to the maximum pressure ratio point at 160 krpm, whereas the former is closer to surge. Analyzing their respective sound intensity spectra in the bottom part of Figure 3, it is obvious that whoosh noise is more prominent at 77 g/s point than at 59 g/s, even though its acoustic intensity integrated in the 1 kHz–2.5 kHz band is lower. This may be the reason why the so-called whoosh noise is more noticeable for the customer in automobile applications in operating conditions

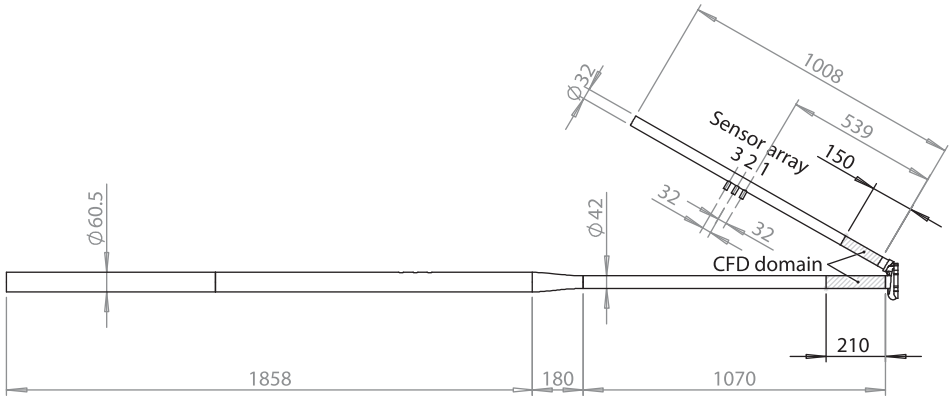


Figure 2. Sketch of compressor piping, highlighting the CFD domain (dimensions in mm).

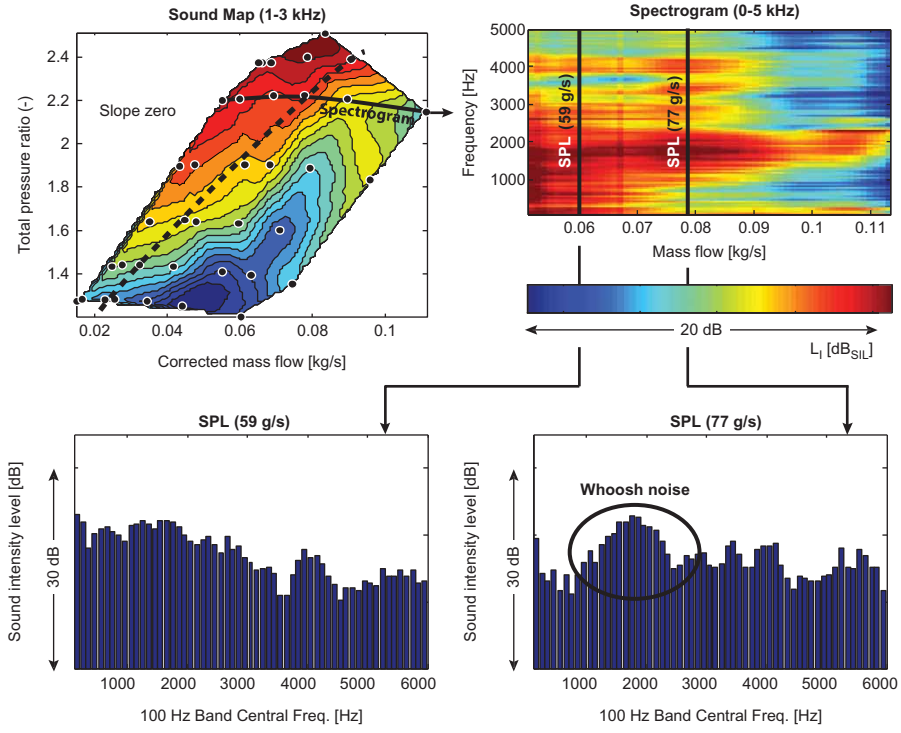


Figure 3. Noise map of the compressor and spectrogram of the 160 krpm isospeed line, including the spectra of two points of interest.

not so close to surge (Evans & Ward, 2006), although the overall noise is not necessarily high.

## 3. Numerical simulations

Measurements described in Section 2 show that, for a speed line, whoosh noise is more relevant for operating conditions corresponding to zero pressure ratio slope than for working points closer to the surge line, as pointed out by Evans and Ward (2006). 3-dimensional CFD simulations using StarCCM+ (CD-adapco, 2013) are performed to investigate the flow at the two operating conditions studied in Section 2.

Numerical simulations are configured following the criteria used by Mendonça et al. (2012). Detached eddy simulations with underlying k-$\omega$ SST turbulence model were performed using the rigid body motion approach. Time-step size was selected for each operating condition causing an impeller rotation of 1° per time step.

The modeled domain is depicted in Figure 4. It includes the vaneless compressor and 5-diameters-long straight inlet and outlet ducts, which were employed to reduce the effect of boundary conditions. Backplate region and tip clearance have been modeled as well. Even though tip gap is expected to decrease from "cold" conditions to actual compressor working conditions, CAD clearance is used in the impeller because a sensitivity analysis carried out by Galindo, Tiseira, Navarro, and López (2015) proves that compressor acoustic signature does not depend on tip clearance ratio.

Figure 4. Modeled domain.

Polyhedral grids are expected to perform with higher accuracy than hexahedral meshes when secondary flows are relevant (Tritthart & Gutknecht, 2013), thus being a common choice for turbomachinery flows (Galindo, Hoyas, Fajardo, & Navarro, 2013; Baris & Mendonça, 2011). Prism layer meshing increases near wall grid resolution so as to obtain $y^+$ values close to the unity in the impeller (see Figure 5). Nine and half million polyhedral cells were used to mesh the domain.

Since the experimental rig described in Section 2 is not entirely modeled for the sake of computational cost (see Figure 2), raw comparison between spectra of numerical

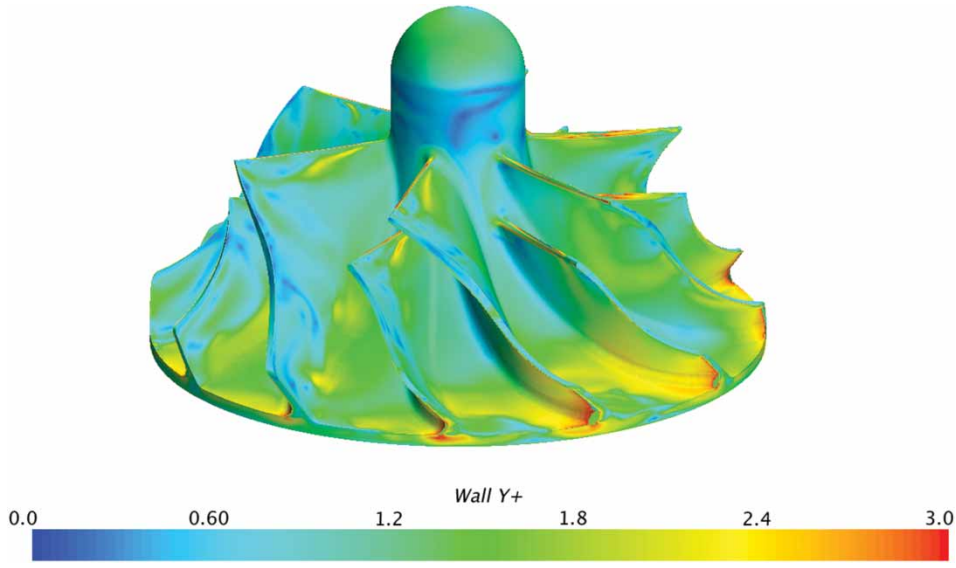


Figure 5. Wall $y^+$ contours at 59 g/s mass flow rate.

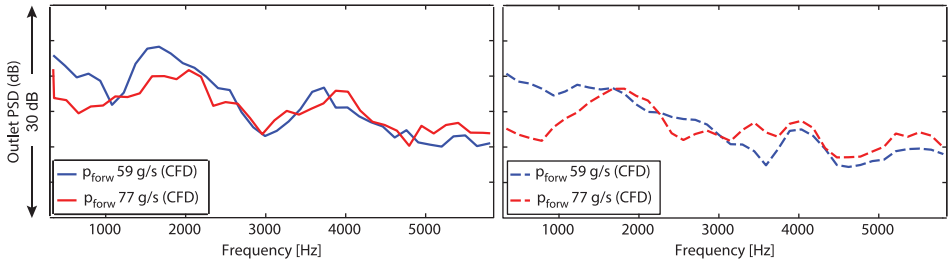


Figure 6. PSD of experimental (left) and numerical (right) forward pressure at outlet duct at 59 g/s (blue) and 77 g/s (red).

and measured pressure signals is not advisable (Broatch, Galindo, Navarro, & García-Tíscar, 2014). Pressure wave decomposition is performed in this study in order to better isolate the spectral information generated specifically by the aeroacoustic sources of the compressor. A pressure record captured in a sole point does not only contain this information, but also includes reflection from the domain boundaries and can even present undesired information from spurious standing waves. Therefore, an array of three pressure probes is placed at inlet and outlet ducts of turbocharger test rig to decompose experimental pressure signals, following again the work of Piñero et al. (2000).

For numerical simulations, pressure decomposition is performed using:

$$p_f = p_0 \left[ \frac{1}{2} \left( 1 + \left( \frac{p}{p_0} \right)^{\frac{\gamma-1}{2\gamma}} \left( 1 + \frac{\gamma-1}{2} \frac{u}{a} \right) \right) \right]^{\frac{2\gamma}{\gamma-1}}$$

$$p_b = p_0 \left[ \frac{1}{2} \left( 1 + \left( \frac{p}{p_0} \right)^{\frac{\gamma-1}{2\gamma}} \left( 1 - \frac{\gamma-1}{2} \frac{u}{a} \right) \right) \right]^{\frac{2\gamma}{\gamma-1}} \quad (2)$$

which are derived in the spirit of the Method of Characteristics, following the same notation as Torregrosa, Fajardo, Gil, and Navarro (2012), i.e., $u$ is the axial velocity, $\gamma$ is the ratio of specific heats and $p$ and $p_0$ are the pressure and reference pressure, respectively. The methodology developed by Broatch et al. (2014) is used as follows: temporal traces of pressure, axial velocity and speed of sound cross-section average are extracted from the simulations, calculating then the pressure components by means of Equation 2.

Power spectral density (PSD) of the forward component of pressure obtained experimentally and predicted by CFD at the outlet duct for both operating conditions are compared in Figure 6. The agreement between measured and modeled signals is quite good. Mean relative error is 2.8% for the 59 g/s case and 2.5% for the 77 g/s case, with the maximum relative error for a particular frequency of about 10% at 3600 Hz for 59 g/s mass flow rate (see Figure 7). Whoosh noise is captured by numerical simulations, i.e., the predominance of pressure amplitude at the range of 1–2.5 kHz is well predicted.

Figure 6 shows that the experimental spectrum monotonously decays from low frequencies until 3.5 kHz for 59 g/s mass flow rate. Then, a narrow band is present from 3.5 kHz to 4.5 kHz and a broadband noise exists until 6 kHz. Instead, the simulation predicts a broadband elevation from 1 kHz to 3 kHz (whoosh noise), even though the decay rate is similar to the measured one. The rest of

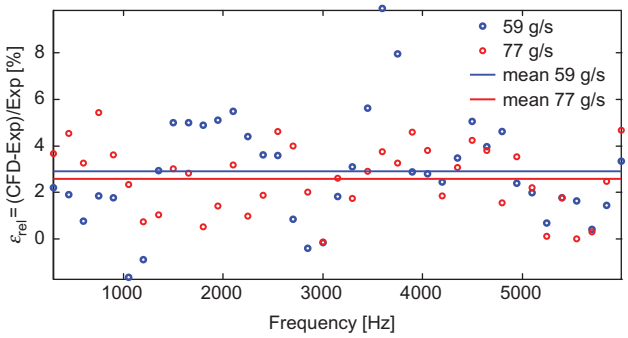


Figure 7. Relative error of forward pressure PSD at outlet duct at 59 g/s (blue) and 77 g/s (red).

the spectrum is similar to the experimental one. For 77 g/s, numerical and measured spectra are very much alike. Whoosh noise is clearly present between 1 and 2.5 kHz, and a broadband noise exists at higher frequencies

Flow is analyzed to detect phenomena occurring at the frequency range of whoosh noise. Figure 8 shows three snapshots of the transient behavior of flow structures at 59 g/s (left side) and 77 g/s (right side). The frames are obtained at three consecutive blade-passing periods. At the impeller inducer, contours of pressure are plotted at two different cross-sections, depicting regions of low pressure (particularly, $p < 85$ kPa). At diffuser midspan, radial velocity magnitude contour is presented, highlighting the level of 100 m/s to facilitate the identification of flow structures.

Flow behavior at the diffuser is quite similar for both operating conditions. The jet-wake structure at the impeller trailing edge is emphasized by the stall cells generated at the blade suction side shown at Figure 9, in which meridional velocity at 50% span is represented using a solid black line to indicate reverse flow. These regions with low momentum are not axisymmetrically distributed. A stalled channel can recover when its low-momentum structure is split and left behind (a close-up of this phenomenon is represented in Figure 10), causing the blockage of subsequent channel. The so-called rotating stall turns at

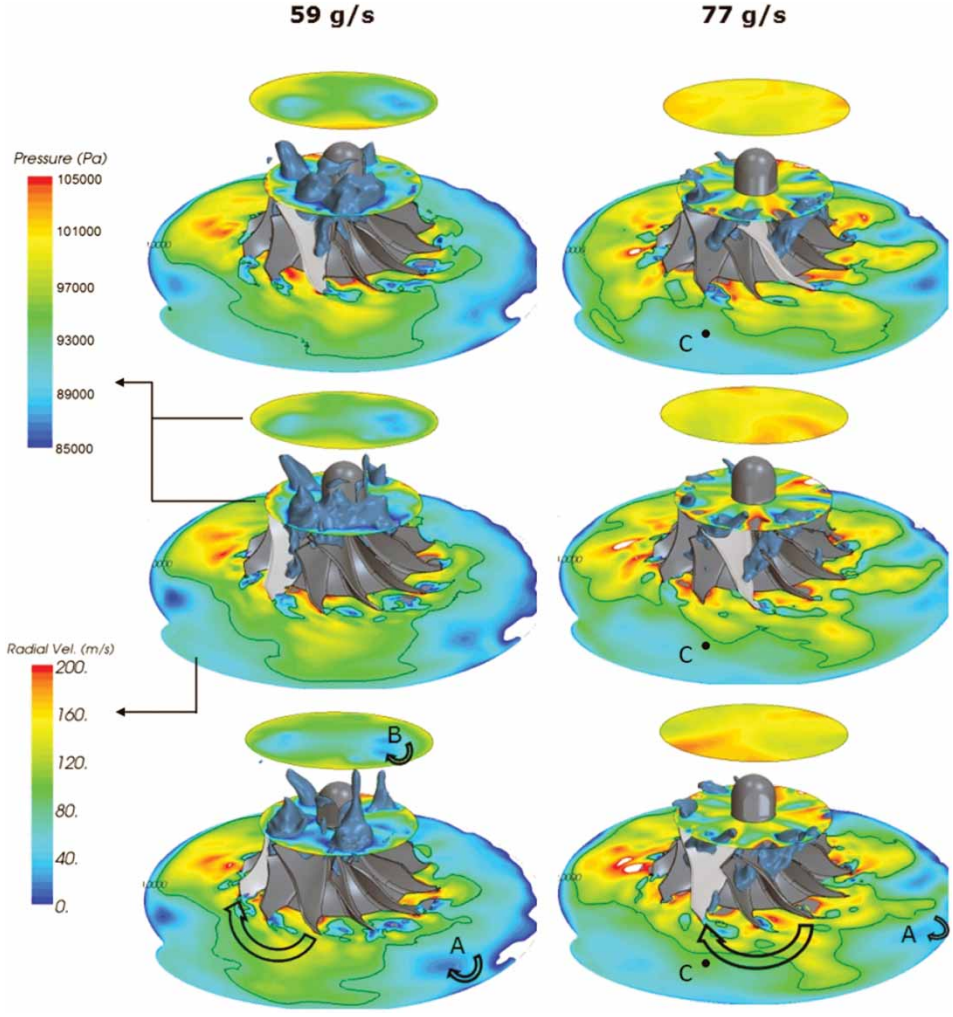


Figure 8. Sequence of snapshots of pressure contours at inducer planes and radial velocity contours at mid-span diffuser for 59 g/s (left) and 77 g/s (right) operating conditions.

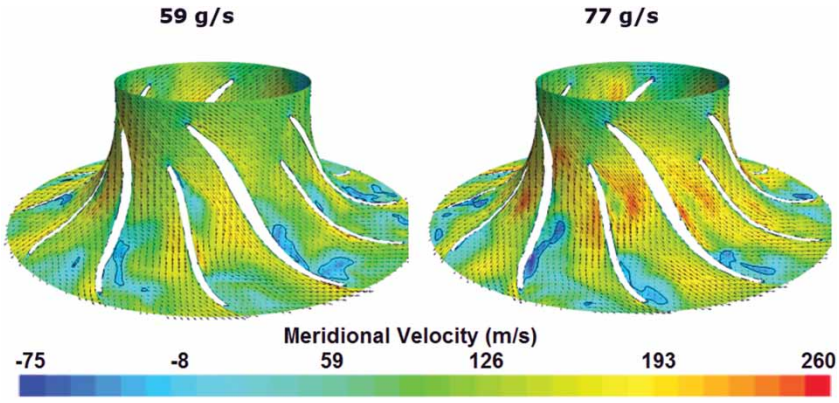


Figure 9. Meridional velocity at 50% span surfaces, at 59 g/s (left) and 77 g/s (right).

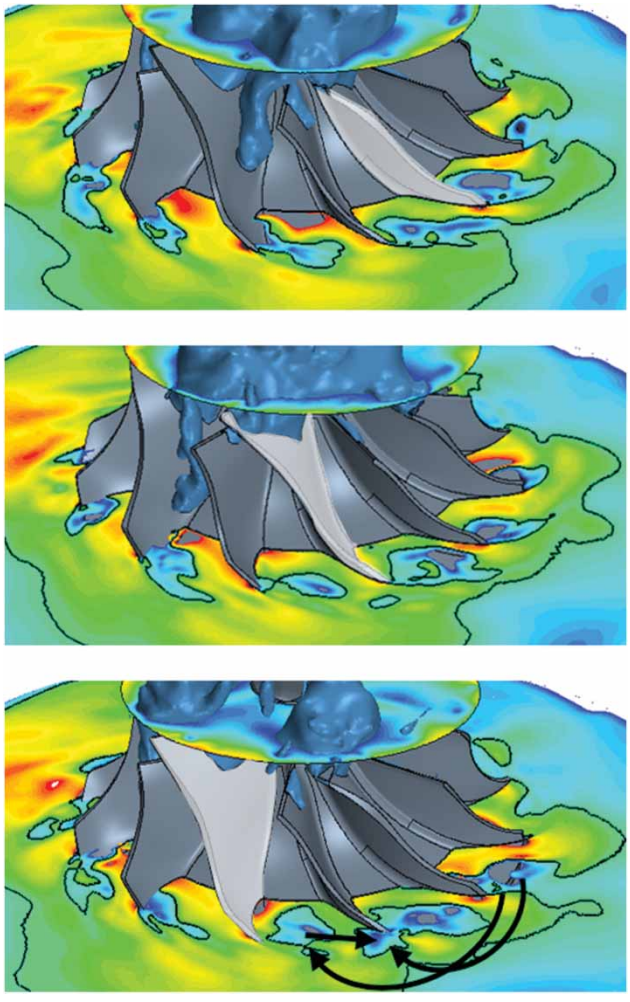

Figure 10. Rotating stall process at impeller trailing edge at 59 g/s.

approximately half the impeller speed (corresponding to 2600 Hz). This phenomenon is responsible for the rotating structures appearing at the diffuser outlet (see A point in Figure 8), which eventually will cause a fluctuating discharge into the volute and outlet duct. So far, diffuser rotating stall is the only phenomenon occurring at the frequency range of whoosh noise, so it may be responsible for this noise.

Several authors (Evans & Ward, 2006; Gaudé et al., 2008; Teng et al., 2009) attributed whoosh noise to turbulence, without going into greater detail. The phenomenon may be related to the so-called tip clearance noise described by Raitor and Neise (2008), but Galindo et al. (2015) found no influence of tip clearance ratio on whoosh noise. Simulations performed by Mendonça et al. (2012) predicted a broadband noise at 70% of impeller rotation frequency, which corresponds to the whoosh noise frequency range. Mendonça et al. ascribed the broadband feature to rotating stall, although their analysis was focused on the inducer flow behavior.

Examination of inducer flow in Figure 8 reveals some differences between operating conditions. Low-pressure regions appear due to flow detachment at the suction side, caused by a bad incidence angle at the blade leading edge. This negative incidence is cause by the low axial component of velocity compared to the rotational component (the operating conditions are close to surge).

At 59 g/s, these low-pressure bubbles are transferred between channels in a similar fashion as their diffuser counterparts. Inducer rotating stall can also be appreciated at the upstream-located cross-section (point B in Figure 8). At 77 g/s, there still exist inducer rotating stall, but with a reduced intensity. In fact, pressure at the upstream plane is quite homogeneous. It should be noted that a difference of 3 kPa exists at this plane between operating conditions because pressure is set as a boundary condition at the outlet, so predicted compression ratio dictates inlet pressure.

Diffuser rotating stall is more intense than inducer rotating stall at operating conditions not so close to surge (77 g/s), where whoosh noise is more prominent, therefore supporting the attribution of compressor whoosh noise phenomenon to diffuser rotating stall. This is in agreement with the observation made by Evans and Ward (2006): the outlet hose contribution to whoosh noise radiation is larger than that corresponding to the inlet duct.

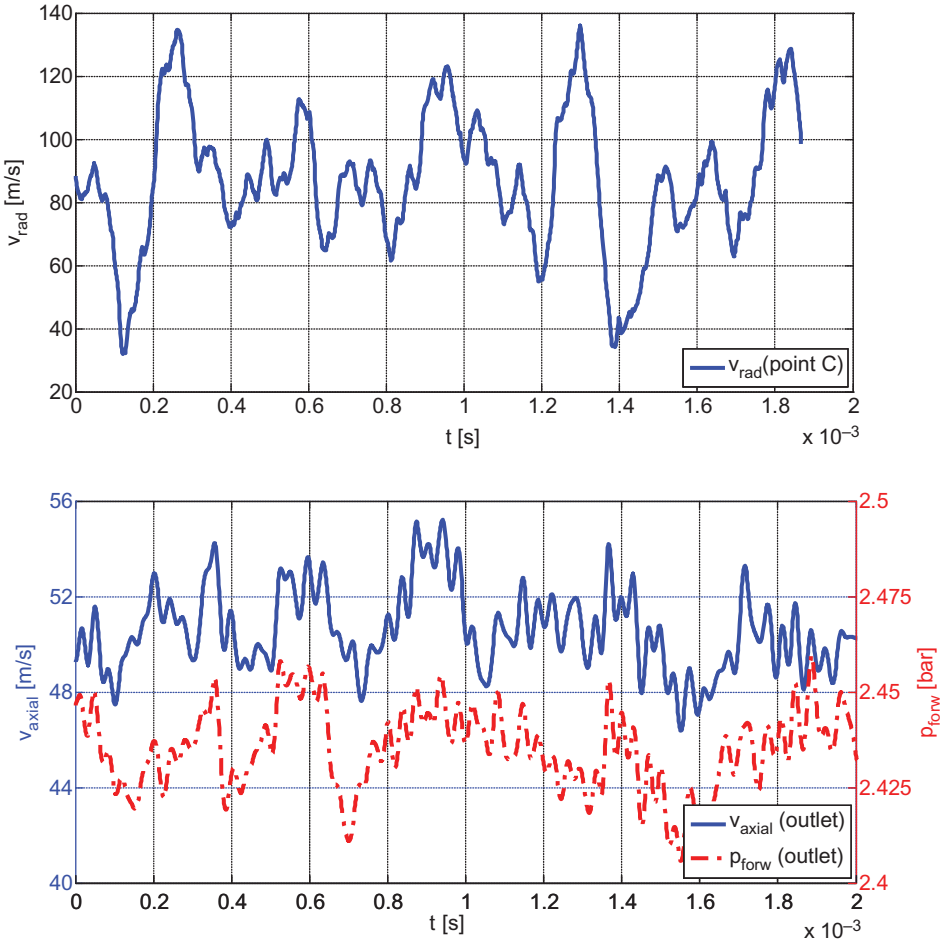


Figure 11. Temporal evolution of radial velocity at point C (top) and axial velocity and forward pressure at outlet cross section (bottom) at 77 g/s.

In order to correlate the fluctuation of radial velocity to the oscillation of pressure in the outlet duct, a point probe is placed at diffuser midspan for 77 g/s mass flow rate case (point C in Figure 8). Figure 11 (top) depicts the evolution of radial velocity at point C, covering a timespan of 2 ms after the compressor reaches a steadily cyclic state. Large fluctuations in the frequency range of whoosh noise can be appreciated. Pressure trace at point C is not representative because it includes all reflections produced at the diffuser. Figure 11 (bottom) is produced considering the outlet cross-sectional surface used in Figure 6 instead. Axial velocity presents low oscillations as in point C, but with a reduced magnitude. Forward pressure is coherent with such fluctuations, which confirms the relation between diffuser rotating stall and whoosh noise.

## 4. Conclusions

In this paper experiments and CFD calculations have been carried out in order to relate flow phenomena to the acoustic signature of a centrifugal compressor operating close to surge. Whoosh noise, which extends from 1 kHz to 2.5 kHz, can be more *relevant* at operating conditions not so close to surge, according to experimental measurements. Two operating conditions at same compressor speed have been examined through calculation: one near the maximum pressure ratio at 160 krpm and the other point closer to surge. Detached eddy simulations of these operating points have been performed, obtaining numerical pressure spectra in agreement with experiments.

The numerical model is used to analyze the flow at these operating conditions, with the objective of identifying aeroacoustic phenomena in the frequency range of whoosh noise (1–3 kHz). Inducer rotating stall is detected, although it is more noticeable when the compressor is working close to surge. Diffuser rotating stall, on the contrary, presents similar intensity for both simulated points, therefore it seems to be the main phenomenon to explain the existence of whoosh noise. Moreover, diffuser rotating stall is located closer to the outlet hose, in which the intensity of whoosh noise is greater. Observation of temporal traces at virtual monitors confirms the coherence between the velocity oscillations at the diffuser due to rotating stall and pressure fluctuations related to whoosh noise in the outlet duct.

The flow behavior during diffuser rotating stall is analyzed, finding flow detachment at the blade suction side, which promote the classical jet-wake structure at the impeller trailing edge. The passages are not evenly loaded, and stall cells travel in the impeller rotation direction at subsynchronous speeds corresponding to the whoosh noise frequency range.

## Acknowledgement

The equipment used in this work has been partially supported by the Spanish Ministerio de Economía y Competitividad through grant no. TRA2012-36954 and by FEDER project funds "Dotación de infraestructuras científico técnicas para el Centro Integral de Mejora Energética y Medioambiental de Sistemas de Transporte (CiMeT), (FEDER-ICTS-2012-06)" framed in the operational program of unique scientific and technical infrastructure of the Spanish Ministerio de Economía y Competitividad.

## ORCID

*R. Navarro* http://orcid.org/0000-0003-2587-4954
*J. García-Tíscar* http://orcid.org/0000-0003-4934-4587

## References

Baris, O., & Mendonça, F. (2011, Jun 6–10). *Automotive turbocharger compressor CFD and extension towards incorporating installation effects*. Proceedings of ASME Turbo Expo 2011: Power for Land, Sea and Air, Vancouver, Canada.

Broatch, A., Galindo, J., Navarro, R., & García-Tíscar, J. (2014). Methodology for experimental validation of a CFD model for predicting noise generation in centrifugal compressors. *International Journal of Heat and Fluid Flow*, *50*, 134–144.

CD-adapco. (2013). *STAR-CCM+ 8.02*, Retrieved from http://www.cd-adapco.com

Evans, D., & Ward, A. (2006, May 17–18). *The reduction of turbocharger whoosh noise*. Proceedings of the 8th International Conference on Turbochargers and Turbocharging, London, UK, pp. 29–42.

Figurella, N., Dehner, R., Selamet, A., Tallio, K., Miazgowicz, K., & Wade, R. (2012, August 19–22). *Noise at the mid to high flow range of a turbocharger compressor*. Proceedings of the 41st International Congress and Exposition on Noise Control Engineering 2012, New York, pp. 786–797.

Galindo, J., Hoyas, S., Fajardo, P., & Navarro, R. (2013). Set-up analysis and optimization of CFD simulation for radial turbines. *Engineering Applications of Computational Fluid Mechanics*, *7*(4), 441–460.

Galindo, J., Tiseira, A., Navarro, R., & López, M. (2015). Influence of tip clearance on flow behaviour and noise generation of centrifugal compressors in near-surge conditions. *International Journal of Heat and Fluid Flow, 52*, 129–139.

Galindo, J., Serrano, J. R., Guardiola, C., & Cervelló, C. (2006). Surge limit definition in a specific test bench for the characterization of automotive turbochargers. *Experimental Thermal and Fluid Science*, *30*(5), 449–462.

Gaudé, G., Lefèvre, T., Tanna, R., Jin, K., McKitterick, T. J. B., & Armenio, S. (2008, October 26–29). *Experimental and computational challenges in the quantification of turbocharger vibro-acoustic sources*. Proceedings of the 37th International Congress and Exposition on Noise Control Engineering 2008, Shanghai, China, pp. 5598–5611.

Karim, A., Miazgowicz, K., Lizotte, B., & Zouani, A. (2013). Computational aero-acoustics simulation of compressor whoosh noise in automotive turbochargers. SAE Paper 2013-01-1880.

Knecht, W. (2008). Diesel engine development in view of reduced emission standards. *Energy*, *33*(2), 264–271.

Lee, I., Selamet, A., Kim, H., Kim, T., & Kim, J. (2009). Design of a multi-chamber silencer for turbocharger noise. *SAE International Journal of Passenger Cars – Mechanical Systems*, *2*(1), 1339–1344.

Mendonça, F., Baris, O., & Capon, G. (2012, June 11–15). *Simulation of radial compressor aeroacoustics using CFD*. Proceedings of ASME Turbo Expo 2012, Copenhaguen, Denmark.

Morfey, C. (1971). Sound transmission and generation in ducts with flow. *Journal of Sound Vibration*, *14*(1), 37–55.

Piñero, G., Vergara, L., Desantes, J. M., & Broatch, A. (2000). Estimation of vel1ocity fluctuation in internal combustion engine exhaust systems through beamforming techniques. *Measurement Science & Technology*, *11*, 1585–1595.

Raitor, T., & Neise, W. (2008). Sound generation in centrifugal compressors. *Journal of Sound and Vibration*, *314*, 738–756.

Semlitsch, B., JyothishKumar, V., Mihaescu, M., Fuchs, L., Gutmark, E., & Gancedo, M. (2014). Numerical flow analysis of a centrifugal compressor with ported and without ported shroud. *SAE Paper* 2014-01-1655.

Serrano, J. R., Margot, X., Tiseira, A., & García-Cuevas, L. M. (2013). Optimization of the inlet air line of an automotive turbocharger. *International Journal of Engineering Research*, *14*(1), 92–104.

Sevginer, C., Arslan, M. O., Sonmez, N., & Yilmaz, S. I. (2007, August 28–31). *Investigation of turbocharger related whoosh and air blow noise in a diesel powertrain*. Proceedings of the 36th International Congress and Exposition on Noise Control Engineering 2007, Instanbul, Turkey, pp. 476–485.

Teng, C., & Homco, S. (2009). Investigation of compressor whoosh noise in automotive turbochargers. *SAE International Journal of Passenger Cars – Mechanical Systems*, *2*(1), 1345–1351.

Torregrosa, A. J., Fajardo, P., Gil, A., & Navarro, R. (2012). Development of a non-reflecting boundary condition for its application in 3D computational fluid dynamic codes. *Engineering Applications of Computational Fluid Mechanics*, *6*(3), 447–460.

Tritthart, M., & Gutknecht, D. (2013). Three-dimensional simulations of free-surface flows using polyhedral finite volumes. *Engineering Applications of Computational Fluid Mechanics*, *1*(1), 1–14.